https://doi.org/10.1016/j.icheatmasstransfer.2019.01.001

CFD modeling of weld pool formation and solidification in a laser micro-welding process

[1]Hozoorbakhsh A., [1,2]Hamdi M., [3]Sarhan A.A.D.M., [4]Ismail M.I.S., [5]Tang C.-Y., [5]Tsui G.C.-P.

[1]Centre of Advanced Manufacturing and Material Processing, Department of Mechanical Engineering, Faculty of Engineering, University of Malaya, Kuala Lumpur, 50603, Malaysia;
[2]Centre for Research in Industry 4.0, University of Malaya, Kuala Lumpur, 50603, Malaysia;
[3]Mechanical Engineering Department, King Fahad University of petroleum and Minerals, Dhahran, 31261, Saudi Arabia;
[4]Department of Mechanical and Manufacturing Engineering, Faculty of Engineering, Universiti Putra Malaysia UPM, Serdang, Selangor 43400, Malaysia;
[5]Department of Industrial and Systems Engineering, The Hong Kong Polytechnic University, Hung Hom, Kowloon, Hong Kong

Abstract

The application of developed thermal models has demonstrated that parameters, such as power, scanning velocity and spot diameter of laser beams have considerable effects on the formation of weld pools. The properties of the weld metal are heavily dependent on the solidification microstructure, and an accurate prediction of the weld pool solidification requires consideration in both the thermodynamics and kinetics of solidification. The computations we presented for a transient three-dimensional model show the aspects of weld pool formation and solidification in a quantitative manner. Our focus was the examination of heat transfer and fluid flow analysis in laser micro-welding of thin stainless-steel sheet (SUS304) using the computational fluid dynamics (CFD) approach. In this research work, a useful linkage between the laser micro-welding parameters and the geometry of the micro-weld can be derived from the results, and informative guidance was achieved as to how the width, depth and length of the weld pool differ during laser micro-welding as a function of spot diameter, scanning velocity and laser power. The simulation results have been compared with two sets of experimental data to predict the weld bead geometry and solidification pattern made on thin stainless steel sheet using a continuous wave (CW) fibre laser. The reasonable agreement between the simulated and experimental results, demonstrates the reliability of the computed model, and the results can be used to determine the laser micro-welding conditions necessary to achieve an appropriate target microstructure. However, the results allow estimation of acceptable ranges of welding variables, to attain the required micro-weld geometry.

Keywords: Laser Micro-Welding; Computational Fluid Dynamics (CFD); Heat Transfer and Fluid Flow Analysis; Weld Pool Formation; Solidification; Thin Stainless Steel Sheet SUS304.

1 Introduction

The earliest study [1] on deep penetration laser beam welding (LBW) was reported in 1971. A brief overview [2] of laser material processing has been summarised. There are several important points in micro beam welding which are essential in the welding process control, including size of beam, beam characterization, interaction of the beam-material, the integration of image processing, temperature measurement and numerical simulation. The scaling effects can be realized which strictly influence the quality of welding such as the cooling rate, solidification structure, fluid flow stability, distortion and surface tension. In addition, laser micro-welding is affected by some important variables in laser such as beam diameter, power of laser, travel speed, beam configuration, condition of the substrate, workpiece thermophysical properties and the alloy composition.

In this regard, the achievements of a study [3] to weld stainless steels in potential applications of laser welding with a pulsed Nd: YAG laser and some studies [4, 5] in laser welding for lightweight structures have been considered. The effect of laser pulse energy, duration and scanning velocity on the dimension of weld, hardness and microstructure during overlapping laser spot welding of low carbon steel using a pulsed Nd: YAG laser have been investigated [6]. It is found that significant variations in the hardness and microstructure of weld in a weld spot could arise in full penetration welding due to the rapid solidification process associated with the technique.

The welding behavior of AISI 304L, 316L and 347 stainless steels with different sheet thicknesses have been discussed [7]. The shape of fusion zone and ultimate solidification microstructure assessed as a laser parameters function. A carbon dioxide laser with 5 kW in CW mode as a highest output power has been applied to make both bead on plate and autogenous butt weld joints. If having the weld joints with perfect penetration, least amount of fusion area size and suitable weld profile production are desired, parameters such as laser power, defocusing distance, welding speed and shielding gas have to be precisely selected depending on the basis of metal thickness.

The ability of physical process simulation using a computer is one of the advances in the last decades. The mathematics governing partial differential equations have made possible solutions to simulate fluid flow, heat transfer and associated processes. The works [8-11] that mainly deal with the simulation of mathematical technique in challenge and development of computational fluid dynamics (CFD), classified in simulation based on finite volume methods (FVM).

A 3-D transient numerical model [12] using FLUENT software has been developed to explore the molten pool shape and temperature field during continuous laser keyhole welding. Some aspects such as recoil pressure, melting and evaporation enthalpy, energy loss because of materials evaporation and surface tension have been considered. The latent heat during melting and solidification was accounted for by employing the enthalpy-porosity technique. The results have shown that the gradients of large temperature take place in the front area of the keyhole. The keyhole formation depends on the recoil pressure, which push the liquid down in the melt pool.

A detailed study on the role of the artificial diffusivity enhancement factors in weld pool simulations, and extended the simulations into the cooling and solidification stage has been reported [13]. It has been shown that during the cooling stage, flow reversal may occur in the weld pool, which enhances the downward heat and momentum transfer. This leads to a deeper weld pool that agrees better with experimental results. By including the cooling and solidification stage into the simulations of weld pool hydrodynamics, an improved agreement with experimentally observed, weld shapes can be obtained with a reduced necessity to artificially enhance the thermal conductivity and dynamic viscosity.

Some primary focus [14, 15] on the numerical computation to solve specific application problems of heat transfer and fluid flow phenomena during laser micro-welding of thin stainless steel sheet have been investigated. A transient 3-D model was developed using CFD method to understand some critical characterisations such as temperature fields and melt pool formation and also the performed parameters of laser micro-welding process. A fair agreement between simulated and experimental results has been shown. The laser's potential understanding is associated with a comprehensive realizing of the physical phenomena in laser welding process with accurate predictions in the heat transport and fluid flow modelling. Thus, some flow and thermal measurements [16, 17] must be applied to refine the models and to extend numerical methods to compute the temperature, velocity, and also measurement of real material property which will give reliable and precise data.

In order to understand the evolution of temperature field, fluid flow and the weld dimensions, the present modelling approach investigates the fundamental aspects of linear laser micro-welding process toward the anatomy of micro-welding, particularly weld pool shape, solidification, heat transfer and fluid flow upon the thin stainless-steel sheet (SUS304) by using a commercial CFD code, ANSYS® FLUENT. In this regard, the effects of laser parameters and welding conditions on the formation of liquid pool were analysed and several important solidification parameters, including solidification rate (R) and temperature gradient (G) at the mushy zone/liquid front, were computed under different laser power, scanning velocity and spot diameter combinations. The temperature field, liquid velocity, melt pool geometry, temperature gradient, the solidification, and cooling rates during micro-welds were compared to each other to better understanding of the processes.

2 Methodology

2.1 Governing equations

In this computational research, melt dynamics analysis, mass conservation, momentum and energy equations were considered in calculating the effects of melt flow and the thermo-fluid energy heat transfer. The mathematical system of partial differential equations (PDEs) for a detailed general-purpose model through the governing equations in three-dimensions, and Newtonian model of the viscous stress resulting in Navier–Stokes equations is developed.

The detailed information [18] about governing equations have been studied and the divergence or conservative form of the equation system that governs the time dependent fluid flow and heat transfer in three-dimensions of compressible Newtonian fluid have been extracted, and quoted as follows:

Continuity:
$$\frac{\partial \rho}{\partial t} + \mathrm{div}(\rho U) = 0 \tag{1}$$

x-momentum:
$$\frac{\partial (\rho u)}{\partial t} + \mathrm{div}(\rho u U) = -\frac{\partial p}{\partial x} + \mathrm{div}(\mu\ \mathrm{grad}\ u) + S_{Mx} \tag{2}$$

y-momentum:
$$\frac{\partial (\rho v)}{\partial t} + \mathrm{div}(\rho v U) = -\frac{\partial p}{\partial y} + \mathrm{div}(\mu\ \mathrm{grad}\ v) + S_{My} \tag{3}$$

z-momentum:
$$\frac{\partial (\rho w)}{\partial t} + \mathrm{div}(\rho w U) = -\frac{\partial p}{\partial z} + \mathrm{div}(\mu\ \mathrm{grad}\ w) + S_{Mz} \tag{4}$$

Energy:
$$\frac{\partial (\rho i)}{\partial t} + \mathrm{div}(\rho i U) = -p\ \mathrm{div}\ U + \mathrm{div}(k\ \mathrm{grad}\ T) + \Phi + S_i \tag{5}$$

2.2 Heat source modelling

The heat source model consists of surface and adaptive volumetric heat sources, which represents the real laser micro-welding as the heat penetrates into the material. It can be observed that the reported values [19-24] of the heat distribution factor in the volume term vary significantly but in the surface are mostly similar. The present work has defined and adapted an improved approach for a moving heat sources by writing specific user-defined functions (UDFs) to perceive continuous laser welding process and applied in both surface and volumetric heat sources as heat flux on top and convection within the weld pool respectively, whereas the weld pool size grows through the framework. Thus, the heat inputs on the top surface and around the molten pool were assumed to have the following adaption Gaussian distributions in the radial direction respectively:

$$Q_S = \frac{fP_S}{\pi {r_d}^2} \exp\left(-3\frac{r^2}{{r_d}^2}\right) \quad (6)$$

$$Q_V = \frac{fP_V}{\pi {r_d}^2 h_d} \exp\left(-3\frac{r^2}{{r_d}^2}\right)\left(1-\frac{z}{h_d}\right) \quad (7)$$

where f is heat distribution factor that influences the power distribution, P_S and P_V are the laser power absorptions in terms of surface and volume respectively, r_d is the beam radius, r is the radial distance from the laser beam centre, z is the current depth in the thickness direction, and h_d is the depth of the energy source. The heat power absorption has been assumed: 25% (P_S) on the substrate surface, and the remained 75% (P_V) by the keyhole wall as shown in Fig. 1.

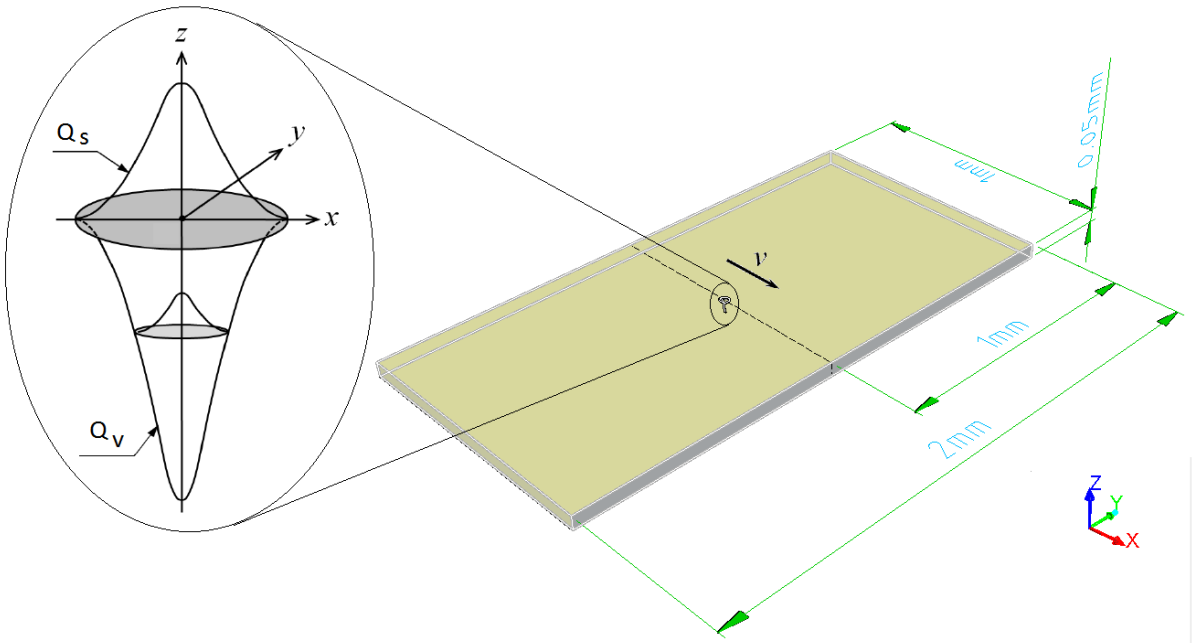

Fig. 1. Heat input model consisting of surface and volume heat sources and geometries used in the CFD model

Bramson's formula [25] was used for calculating absorptivity/reflectivity based on laser wavelength. The reported value [14, 15] indicated the absorption rate of fibre laser is 0.27 for the SUS304 without coating.

2.3 Assumptions

The basic assumptions to develop the model were as follows:

- The liquid metal in the weld pool was assumed Newtonian, incompressible, transient and laminar flow.
- To simplify the model and expedite the computations, the model was premeditated symmetrical in the middle of the specimen and only half of the model was solved.
- The weld pool surface was assumed to be flat.
- The effect of plasma was ignored for simplicity.
- The effect of radiation heat transfer was negligible and only conductive and convective heat transfer was modelled.
- Thermophysical material properties such as thermal conductivity, specific heat and density were assumed temperature dependent, isotropic and homogeneous.

2.4 Computational approach

A transient 3-D simulation model of laser micro-welding was performed using ANSYS® FLUENT software based on pressure-based Navier-Stokes solution algorithm to investigate the heat transfer and fluid flow analysis. To obtain both conduction and keyhole modes laser welding, six processing conditions with various laser powers, scanning velocities and spot diameters have been chosen as shown in Table 1.

Table 1. Laser parameters and welding conditions

Case	**1**	**2**	**3**	**4**	**5**	**6**
Laser power (*P*, W)	20	30	40	20	40	60
Scanning velocity (*v*, m/s)	1.0	1.5	2.0	0.5	1.0	1.5
Spot diameter (*d*, μm)	17.5	17.5	17.5	35.0	35.0	35.0

ANSYS Fluent is able to solve governing equations of fluid flow and heat transfer in a time-dependent manner to analyse some time-dependent phenomena, e.g. transient heat convection and conduction. The model is capable to change by the simple alteration of different operational parameters such as dimension, welding speed and material property in order to simulate various welding conditions.

The size of the specimen was 2 mm × 1 mm × 50 μm. The coordinate system and the computational domain type utilised in this simulation are also illustrated in Fig. 1.

Basically, there were two types of 3-D structured mesh blocks allocated in this model whereby the first one consisted of 1,480,000 hexahedral cells, for cases with 35.0 μm spot diameter and the second one having 1,300,000 hexahedral cells, to consider other cases with 17.5 μm spot diameter. The smallest mesh size was 1μm. In order to have better efficiency and accuracy, the meshes close to the heat source and regions in contact with the laser beam were designed denser as they experience a complex thermal

sequence of momentary heating and cooling in the vicinity of the top and bottom surfaces and thickness. In the other areas outside the heating zone, coarse meshes were employed, whereas the mesh size increased exponentially across the longitudinal of the workpiece. This mesh pattern was useful to attain both the accurate results and reduction of simulation time.

The piecewise-polynomials [26] were selected to define material properties as a function of temperature to set the density, constant-pressure specific heat, thermal conductivity and viscosity of the material and also the constant values of pure solvent melting heat that specifies the latent heat and the liquidus and solidus temperatures in accordance with Fig. 2 and Table 2.

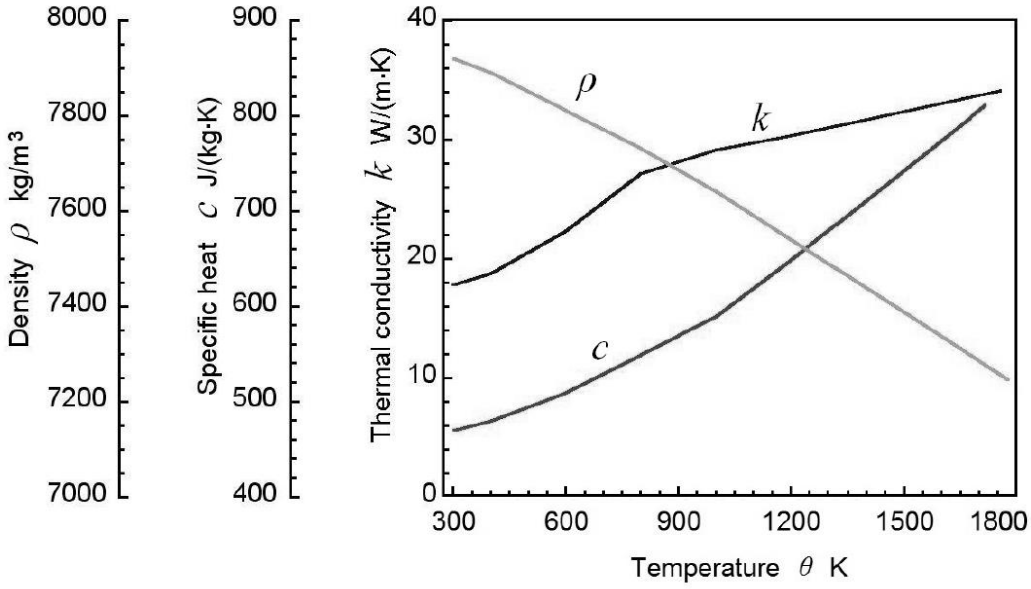

Fig. 2. Thermophysical properties of austenitic stainless steel SUS304 [14, 15]

Table 2. Material physical properties of austenitic stainless steel SUS304

Property	Symbol	Value	Unit
Ambient temperature	T_∞	293	K
Solidus temperature	T_s	1670	K
Liquidus temperature	T_m	1720	K
Boiling temperature	T_v	3200	K
Pure solvent melting heat	ΔH	2.5×10^{5}	J kg^{-1}
Sensible enthalpy	h	10	W m^{-2} K^{-1}
Dynamic viscosity	μ	0.1	kg m^{-1} s^{-1}
Thermal expansion	α	4.95×10^{-5}	K^{-1}

2.5 Cell zone and boundary conditions

In this model, three wall boundaries were defined as welding_wall, bottom_wall and side_walls to adjust the parameters of boundary condition. The welding_wall contained the top surface in the physical geometry, and was considered a moving wall in the wall motion category which enables the tangential wall speed specification. The application of tangential wall motion was only for viscous flows. The Relative to adjacent cell zone was enabled to specify wall velocity. Translational was also enabled to specify translational wall velocity in the *x*-direction. Specified shear was enabled to specify Shear condition. The heat flux option under Thermal Conditions was chosen for a fixed heat flux condition. It was needed to adjust the suitable value for the heat flux at the wall surface in the heat flux field. It could be defined an adiabatic wall by adjusting a zero heat flux condition which can be the default condition for all walls. In this model, a UDF was coded to calculate surface heat source (Q_S) known as heat flux boundary condition made by the laser beam operated on the top surface of the specimen. Source terms can be defined as volumetric sources of mass, energy, momentum and other scalar quantities in a fluid area in cell zone conditions. This characterisation was helpful to input an identified value for these sources. This UDF could be created for more complex sources with functional dependency. Herein a volume heat source of energy (Q_V) was created through defining another UDF as source terms in fluid zone, as it explained before. The bottom_wall and side_walls were contained the bottom surface and outer surfaces in the physical geometry of specimen respectively, with the same setting up the boundary conditions for a wall zone in comparative wall dialog boxes. Momentum category that displays the momentum boundary conditions was specified the walls were not moving relative to the fluid adjacent cell zone and determined as a stationary wall in the wall motion task. Shear condition at the both walls was specified a no-slip condition at the walls and no more inputs were required. The convection under thermal condition was selected as convective heat transfer boundary condition model type. Heat transfer coefficient (Sensible enthalpy) and free stream temperature (Ambient temperature) for both the bottom_wall and side_walls were assumed 10 W m^{-2} K^{-1} and 293 K respectively.

2.6 Experiment details

The experimental results [19] of this laser micro-welding process have been obtained by employing a single-mode CW fibre laser with the high-speed scanning system in the bead-on-plate welding condition. The wavelength of 1090 nm single-mode CW Yb fibre laser has been used. The laser has been delivered by optical fibre and focused by a telecentric type $f\theta$ lens of 100 mm in focal length. The laser scanning has been carried out by a Galvano scanner to achieve the high-speed beam scanning. The expander has been installed to change the diameter of laser beam. In addition, the experiments with

bead-on-plate welding have been carried out in shielding gas of nitrogen under a constant pressure of 100 kPa.

The clamping plate with an opening slot of 2 mm was set to ensure the straighten of specimen sheets. The groove was prepared under the specimen to keep the non-contact space between the specimen and the clamping plate. In addition, the alumina-ceramic plates of 1 mm thickness were located between specimen and clamping plate to minimize the heat loss during welding experiments. After the laser welding, the welded specimens were cut perpendicular to the scanning direction for the observation of weld bead by optical microscope. All the specimens were ground and polished. Etching was performed using a solution containing 4 ml HNO_3, 16 ml HCl, 12 ml $C_6H_3N_3O_7$ (5%) and 10 ml distilled water for 3 seconds.

3 Results and discussion

3.1 Weld pool shapes

The computed critical sizes such as length, width and depth which define the liquid pool size and its shape using the contours of total temperature (melting point and above) under different laser power, scanning velocity and spot diameter combinations during laser micro-welding process are shown in Fig. 3 – Fig. 8 in both top and side views. Note that, temperature of 1720 K is considered as the melting point of SUS304. Every cell is equal to 1 μm^3 which represents the smallest mesh size as well.

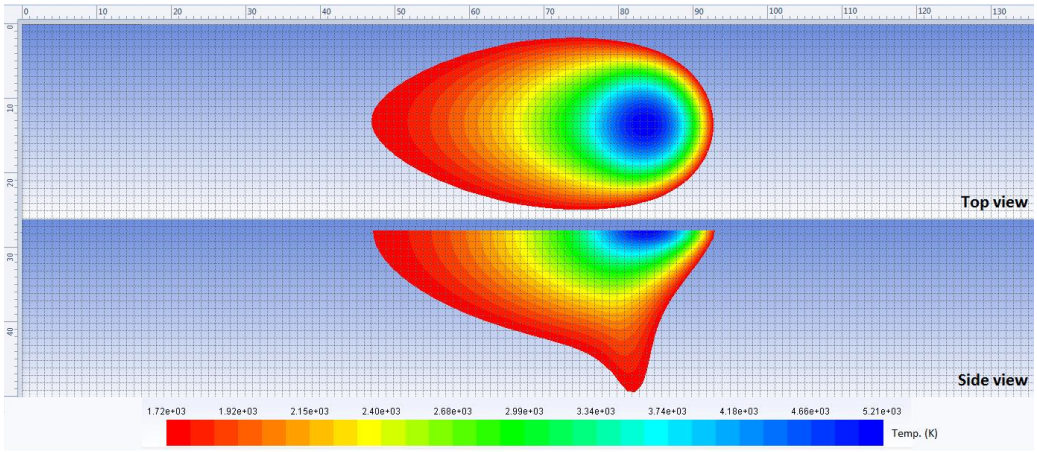

Fig. 3. Computed length, width and depth of the weld pool using contours of total temperature (Case 1: *P*=20 W, *v*=1 m/s, *d*=17.5 µm)

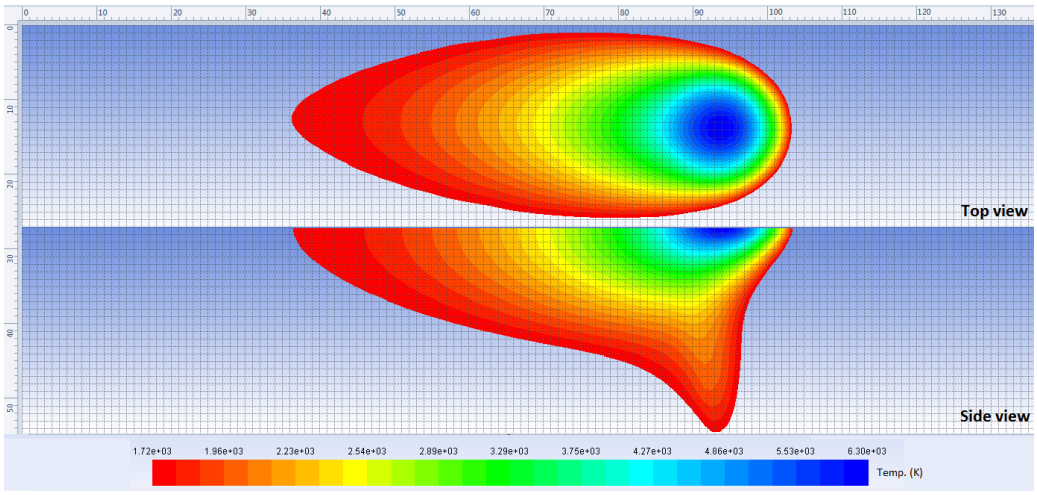

Fig. 4. Computed length, width and depth of the weld pool using contours of total temperature (Case 2: *P*=30 W, *v*=1.5 m/s, *d*=17.5 µm)

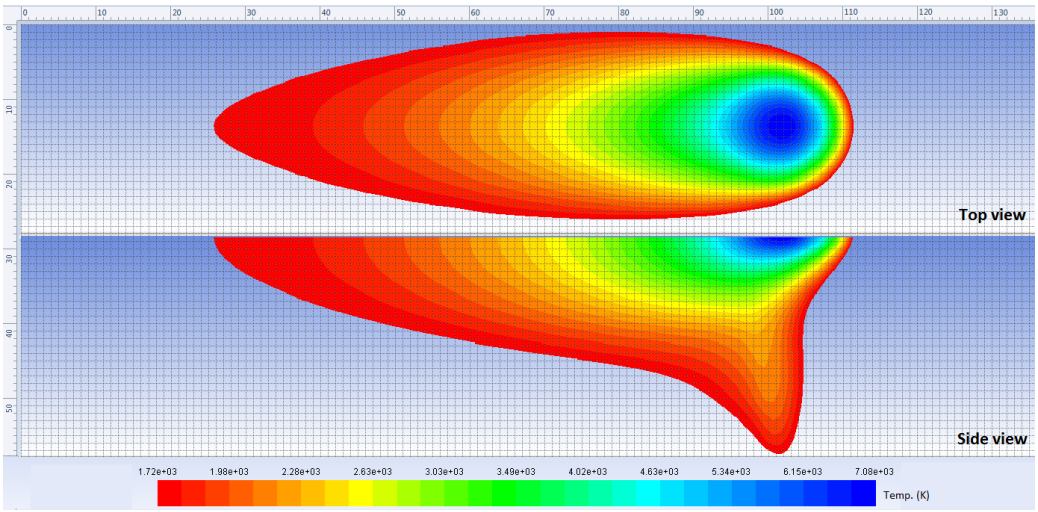

Fig. 5. Computed length, width and depth of the weld pool using contours of total temperature (Case 3: *P*=40 W, *v*=2 m/s, *d*=17.5 μm)

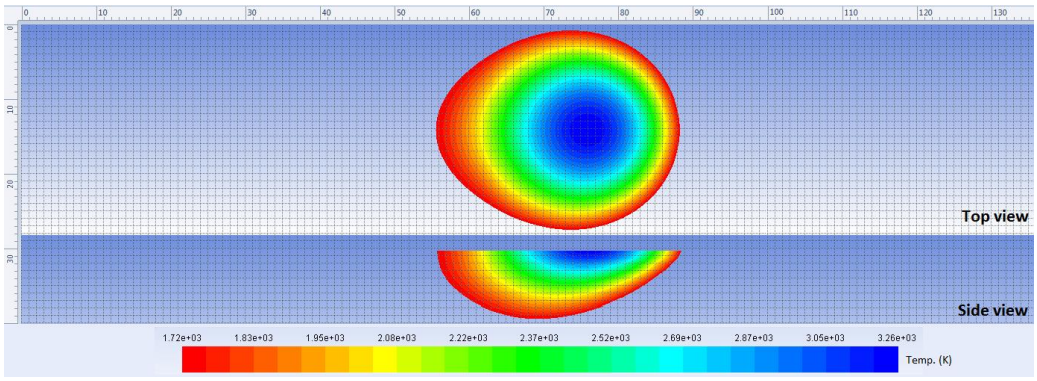

Fig. 6. Computed length, width and depth of the weld pool using contours of total temperature (Case 4: *P*=20 W, *v*=0.5 m/s, *d*=35 μm)

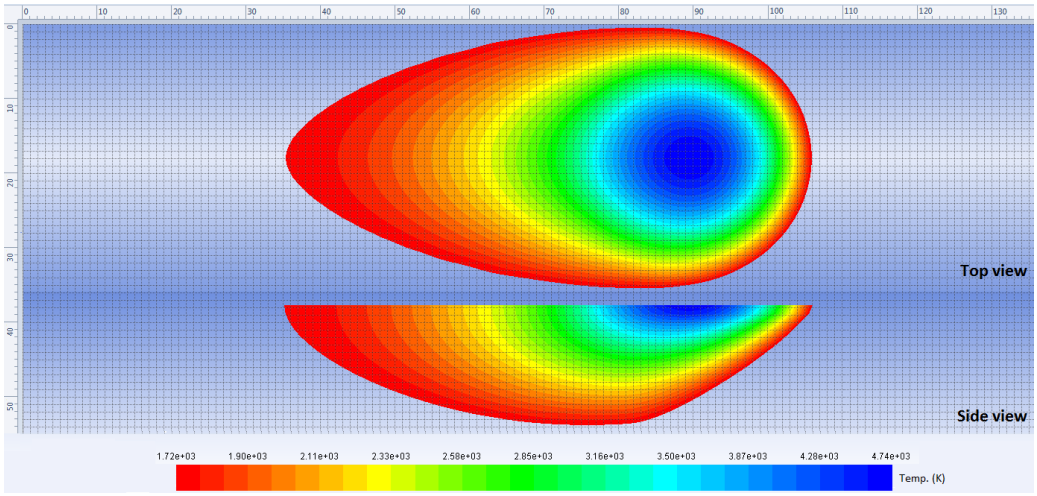

Fig. 7. Computed length, width and depth of the weld pool using contours of total temperature (Case 5: *P*=40 W, *v*=1 m/s, *d*=35 μm)

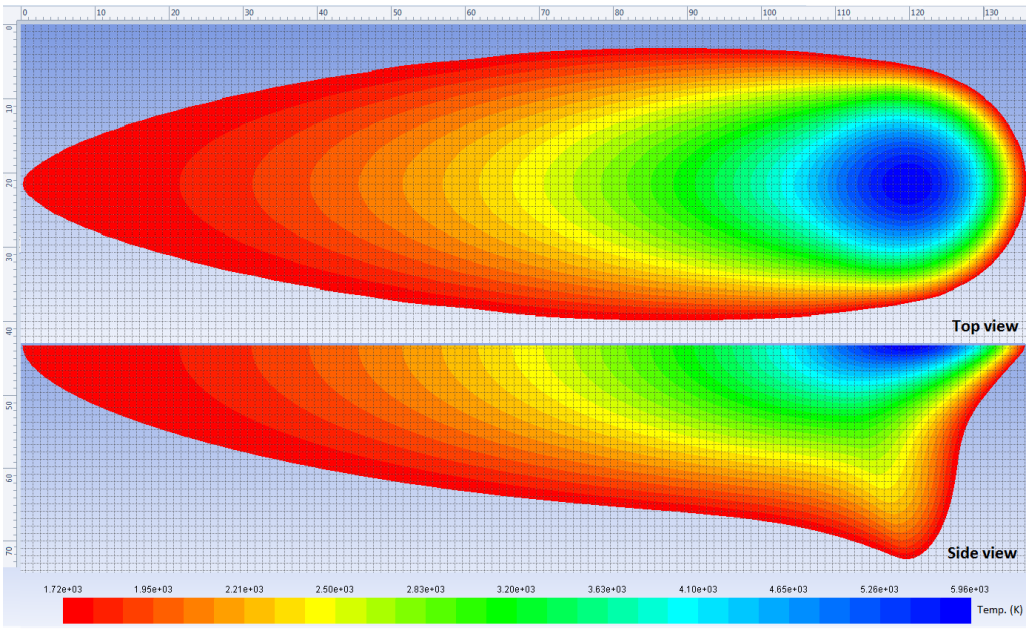

Fig. 8. Computed length, width and depth of the weld pool using contours of total temperature (Case 6: *P*=60 W, *v*=1.5 m/s, *d*=35 μm)

As can be seen from Fig. 3 to Fig. 8, the weld pool becomes more elliptical shape for faster scanning velocity and higher laser power. In addition, the weld pool shape of bigger spot diameter with slower scanning velocity and lower laser power led to the circular weld pool shape. The wider laser beam diameter covers up a broad area on the top surface of the specimen whereas a shallower liquid pool is generated. This condition can be considered as the conduction mode welding, while the smaller spot diameter is leading up to the keyhole mode welding.

The variations of measured maximum total temperature, maximum liquid metal velocity and molten pool measurements (length, width and depth) with various laser power, laser velocity and laser beam diameter are shown in Table 3.

Table 3. Maximum total temperature, liquid velocity and weld pool size (length, width and depth) in different laser parameters and welding conditions

Cases	Temp. (K)	Liquid velocity (m/s)	Weld pool length (μm)	Weld pool width (μm)	Weld pool depth (μm)
Case 1 (P=20 W, v=1 m/s, d=17.5 μm)	5210	0.309	46	23	22
Case 2 (P=30 W, v=1.5 m/s, d=17.5 μm)	6300	0.668	67	25	28
Case 3 (P=40 W, v=2 m/s, d=17.5 μm)	7080	1.170	86	25	29
Case 4 (P=20 W, v=0.5 m/s, d=35 μm)	3260	0.0 69	33	26	9
Case 5 (P=40 W, v=1 m/s, d=35 μm)	4740	0.265	71	35	16
Case 6 (P=60 W, v=1.5 m/s, d=35 μm)	5950	0.544	135	37	33

The computed results reported in Table 3 demonstrate that both the maximum velocity and temperature of the liquid metal are increased by the laser power increment and the increased laser power results in more penetration. Fig. 3 - Fig. 8 and Table 3 represent that, at a constant laser power, e.g., cases 1 and 4 or 3 and 5, the smaller size of laser beam leads to deeper weld pool, upper liquid velocity and higher peak temperature because of the higher power density of laser. It is noticeable that the power density has to be high enough to melt the regions exactly under the laser beam. In contrast, with the rising of beam diameter from 17.5 to 35 μm, lower liquid velocity and peak temperature are yielded and consequently the width of weld pool is increased and the weld pool depth is decreased.

A significant characteristic of the results is that, a multiple combination of welding variables contributes to a particular weld attribute e.g., the weld penetration. The existence of numerous paths to obtain a preferred weld attribute represents the flexibility in the laser micro-welding process.

3.2 Solidification

The properties of the resultant weld depend on the solidification microstructure that is affected by the solidification rate (R), temperature gradient (G), undercooling (ΔT), and the alloy composition [27, 28] . In this study, some of the solidification parameters were calculated by considering the heat transfer and fluid flow in the weld pool, during laser micro-welding process. The solidification rate

varied with position along the fusion boundary. This point is shown schematically in Fig.9 using the contours of adaption space gradient based on the solidification/melting (Liquid Fraction) computation in case 1 (Fig.10).

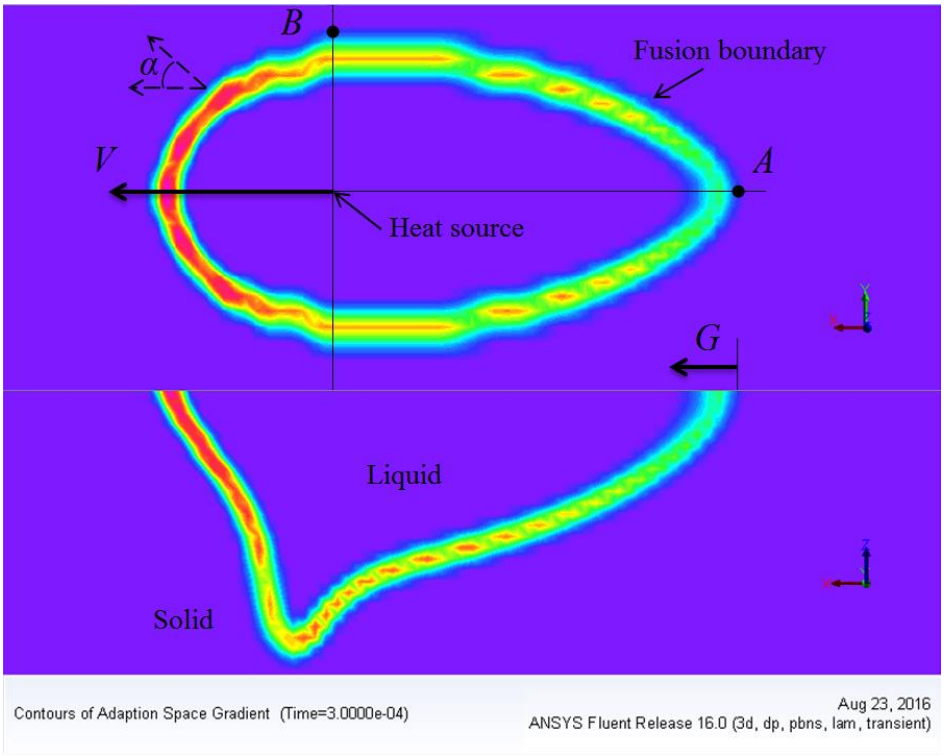

Fig. 9. Schematic of the weld pool shape using contours of adaption space gradient based on the solidification/melting (Liquid Fraction) simulation from top and side views (Case 1: *P*=20 W, *v*=1 m/s, *d*=17.5 µm)

As can be seen, the direction of movement of the solidification front is along the maximum thermal gradient normal to the solid/liquid interface. Accordingly, the solidification rate (R) is related to the welding speed as follows:

$$R = V \cos \alpha \tag{8}$$

where α is the angle between the normal to the solid/liquid interface and the welding direction and V is the welding speed. The solidification rate is the highest at point A on the weld centreline because the interface normal has the same direction as the welding direction and it is lowest at the edge of the weld pool ($\alpha \rightarrow 90° \Rightarrow \cos \alpha \rightarrow 0$) indicated by point B in Fig. 9. The solidification rate decreases from point A to point B along the fusion boundary [28, 29]. To consider the solidification rate (R) at the mushy zone/liquid interface, the computed values of liquid fraction and adaption space gradient based on liquid fraction contour are illustrated in a symmetrical melt pool (Fig. 10).

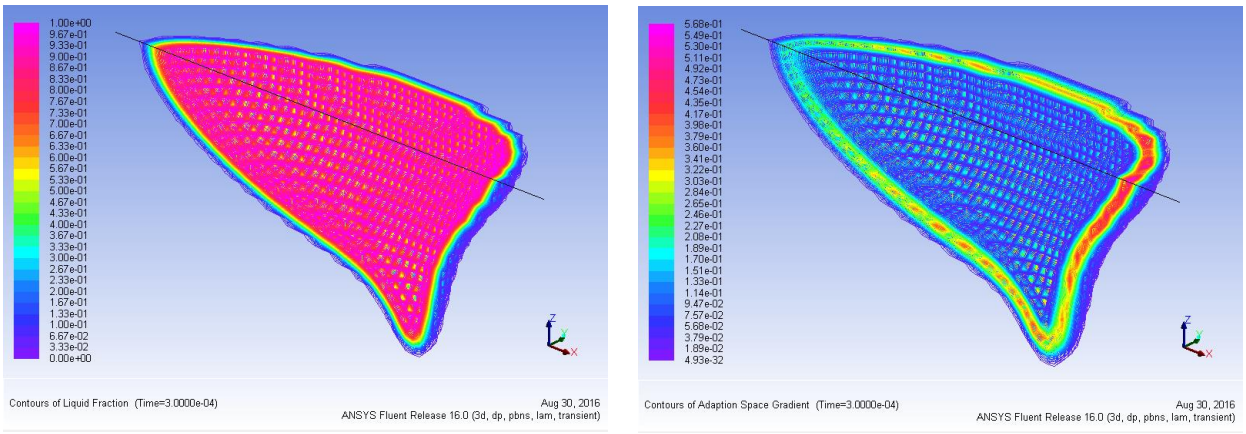

Fig. 10. Contours of liquid fraction and adaption space gradient based on liquid fraction contour in a half-width liquid pool of a typical case (Case 1: *P*=20 W, *v*=1 m/s, *d*=17.5 µm)

The temperature gradient (G) and the solidification rate (R) are important in the combined forms GR and G/R as they affect the scale of the solidification substructure and the solidification morphology respectively. As the value of G/R increases, the interface morphology changes from equiaxed-dendritic, to cellular-dendritic or to cellular grains. Often the value of G/R close to the fusion line is large enough to facilitate cellular solidification. As the temperature gradient in the weld pool decreases with distance from the fusion boundary, the solidification microstructure may vary spatially. For instance, in some cases, an equiaxed-dendritic microstructure at the weld pool centre and a cellular-dendritic microstructure (mushy zone/liquid interface) between fusion boundary and weld centreline can be obtained [28, 29]. Fig. 11 shows the computed results of static temperature and adaption space gradient based on static temperature contour in a symmetrical weld pool as in case 1. Furthermore, in Fig. 12, the solution XY plots of adaption space gradient based on static temperatures in six different cases have been used to calculate the maximum temperature, gradient temperature *(G)* and consequently GR and G/R as functions of solidification parameters.

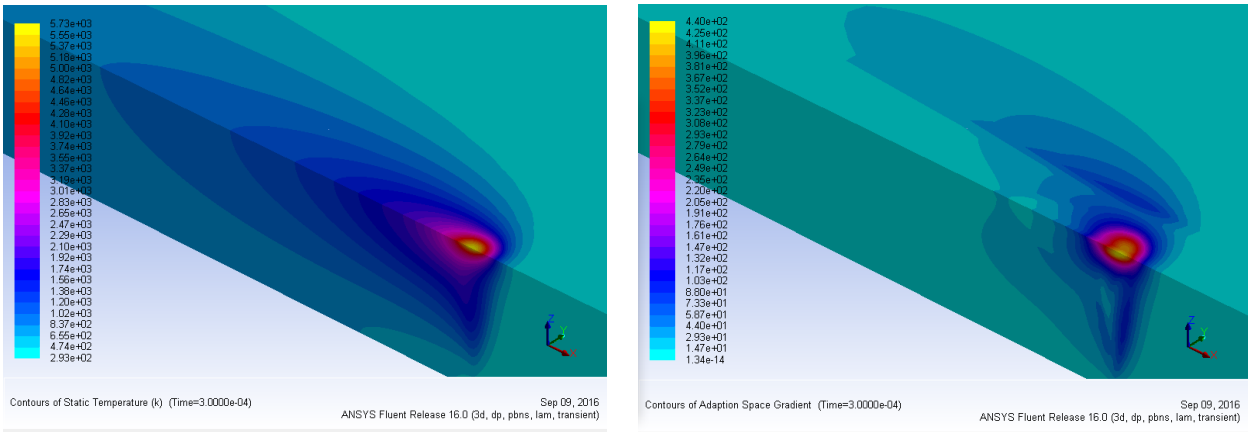

Fig. 11. Contours of static temperature and adaption space gradient based on static temperature contour in a half-width weld pool of a typical case (Case 1: *P*=20 W, *v*=1 m/s, *d*=17.5 µm)

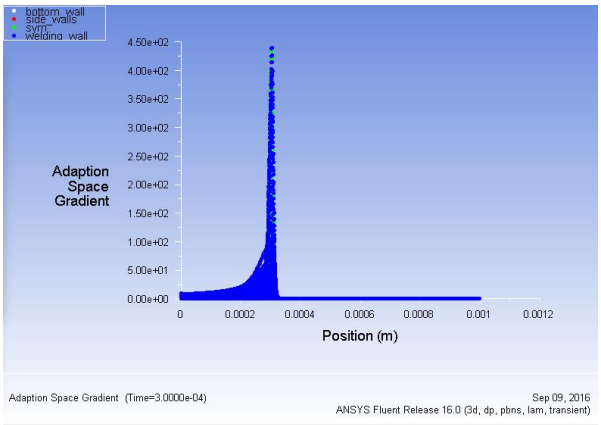

Case 1: *P*=20 W, *v*=1 m/s, *d*=17.5 µm

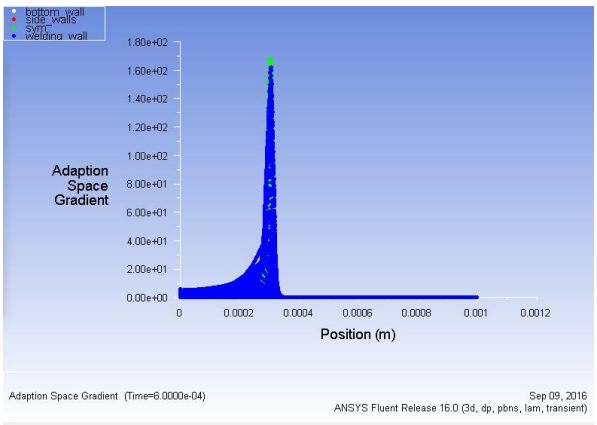

Case 4: *P*=20 W, *v*=0.5 m/s, *d*=35 µm

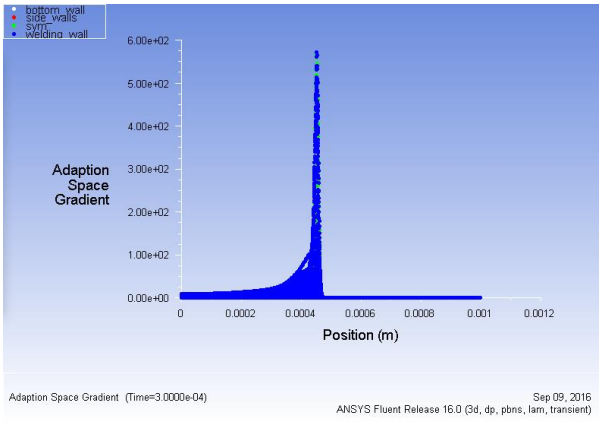

Case 2: *P*=30 W, *v*=1.5 m/s, *d*=17.5 µm

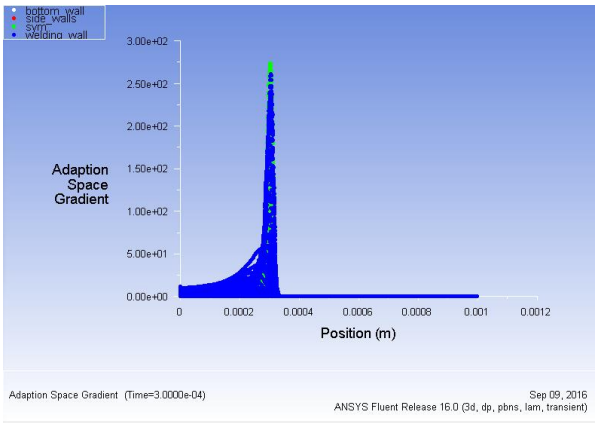

Case 5: *P*=40 W, *v*=1 m/s, *d*=35 µm

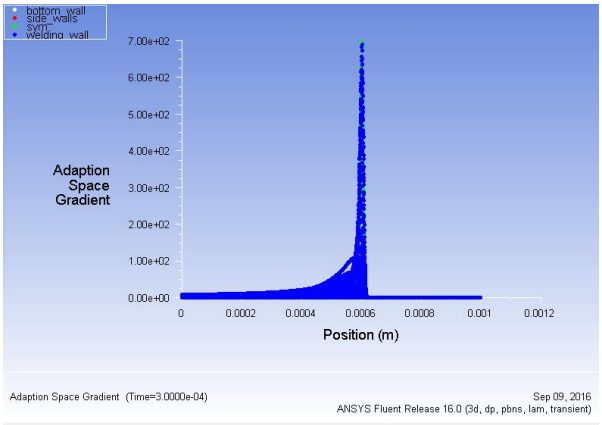

Case 3: *P*=40 W, *v*=2 m/s, *d*=17.5 µm

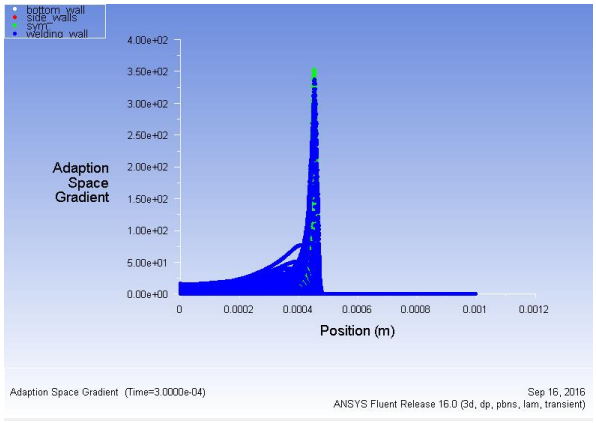

Case 6: *P*=60 W, *v*=1.5 m/s, *d*=35 µm

Fig. 12. Comparison between calculated solution XY plots of adaption space gradient based on static temperatures in different cases with various laser parameters and welding conditions

The cooling rate significantly affects the microstructure and properties of the welds. The weld cooling rates in laser welding are normally high, often in the range of 10^4–10^6 °C/s. Cooling rates in welding are mostly compared by calculating the time taken from 800 to 500 °C (Δt_{8-5}). The austenite to ferrite phase transformation takes place in this temperature range in plain carbon steels. Although less significant for other alloys, Δt_{8-5} gives a convenient parameter to compare cooling times [28]. Fig. 13

exhibits the computed cooling rate from the heat transfer and fluid flow model as a function of welding speed in laser micro-welding that Δt_{8-5} has been calculated by dividing the x distance between contour lines of 1073 and 773 K with welding speed, in a symmetrical weld pool (case 4). The measurement of cell unit is μm and the smallest mesh size is 1 μm^2, hereon every cell is equal to 2.5 μm^2.

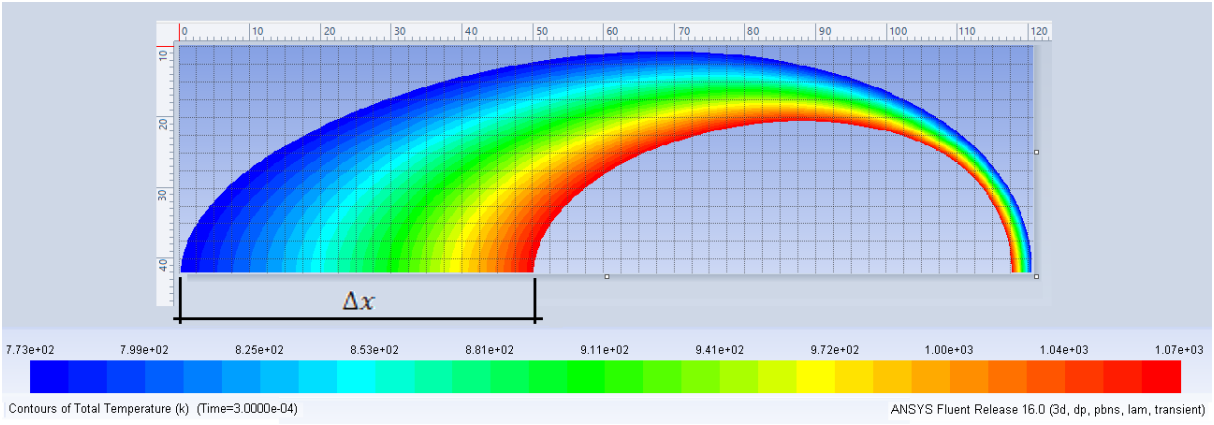

Fig. 13. Computed cooling time (Δt_{8-5}) from 1173 K to 773 K using contours of total temperature in a half-width weld pool (Case 4: *P*=20 W, *v*=0.5 m/s, *d*=35 μm) from top view

The calculated values of maximum static temperature (peak temperature) and solidification parameters including; solidification rate (R), temperature gradient (G), scale of the solidification substructure, (GR) solidification morphology (G/R) and cooling rate (Δt_{8-5}) at the weld centreline in laser micro-welding that were simulated by varying laser power, scanning velocity and spot diameter in different cases are presented in Table 4.

In Table 4, the higher values of peak were obtained by decreasing the spot diameter from 35 to 17.5 μm and the maximum laser beam power of 40 W. It is shown that with the increase in laser power which resulted in higher laser power density; the temperature gradient is increased steadily, the values of GR and G/R increased and decreased respectively at the weld centreline in both spot diameters. Thus the scale of the solidification substructure and the solidification morphology of the fusion zone would be influenced by modifying the laser power and laser beam diameter during laser micro-welding process.

Table 4. Comparison between maximum static temperature, solidification rate (*R*), temperature gradient (*G*), solidification morphology (*G*/*R*), scale of the solidification substructure (*GR*) and cooling rate (Δt_{8-5}) in different cases

Different Cases	Temp. (K)	*R* (μm/ms)	*G* (K/μm)	*GR* (K/mm)	*G*/*R* (Kms/μm^2)	Δt_{8-5} 1073 to 773 K (ms)
Case 1 (*P*=20 W, *v*=1 m/s, *d*=17.5 μm)	5730	0.001	440	440000	0.44	0.104
Case 2 (*P*=30 W, *v*=1.5 m/s, *d*=17.5 μm)	6960	0.0015	572	381333	0.858	0.106
Case 3 (*P*=40 W, *v*=2 m/s, *d*=17.5 μm)	7900	0.002	697	348500	1.394	0.107
Case 4 (*P*=20 W, *v*=0.5 m/s, *d*=35 μm)	3420	0.0005	169	338000	0.085	0.10
Case 5 (*P*=40 W, *v*=1 m/s, *d*=35 μm)	5000	0.001	274	274000	0.274	0.173
Case 6 (*P*=60 W, *v*=1.5 m/s, *d*=35 μm)	6280	0.0015	353	235333	0.530	0.223

The computed results show that the cooling rate (Δt_{8-5}) is associated with laser power resulted to the maximum temperatures in both 17.5 μm and 35 μm spot diameters and also it is increased slightly by increasing the laser welding speed (Scanning velocity). It should be noted that since both the cooling rate (Δt_{8-5}) and the solidification rate (*R*) grow by increasing the power and speed of laser, the variation of temperature gradient (*G*) with them is not monotonous. Depending on how the cooling rate and solidification rate change with power, speed and diameter of laser beam, the value of the temperature gradient can either increase or decrease.

In this study, the results shown in Fig. 12, Fig. 13 and Table 4 indicate that the temperature gradient decreases or increases by the amount of laser power density in conjunction with laser power and laser beam diameter size and it is not much influenced by the welding speed. It seems that the velocity of laser movement is insignificant, based on the selected welding conditions.

3.3 Comparison between simulation and experimental data

The comparison between simulated liquid fraction and experimental data in case of weld bead geometry in cross-sectional view and solidification pattern from top view are demonstrated in Fig. 14 and Fig. 15, respectively. The computed melting/solidification concept that considered the contours of liquid fraction is used to predict the weld bead geometry and solidification pattern.

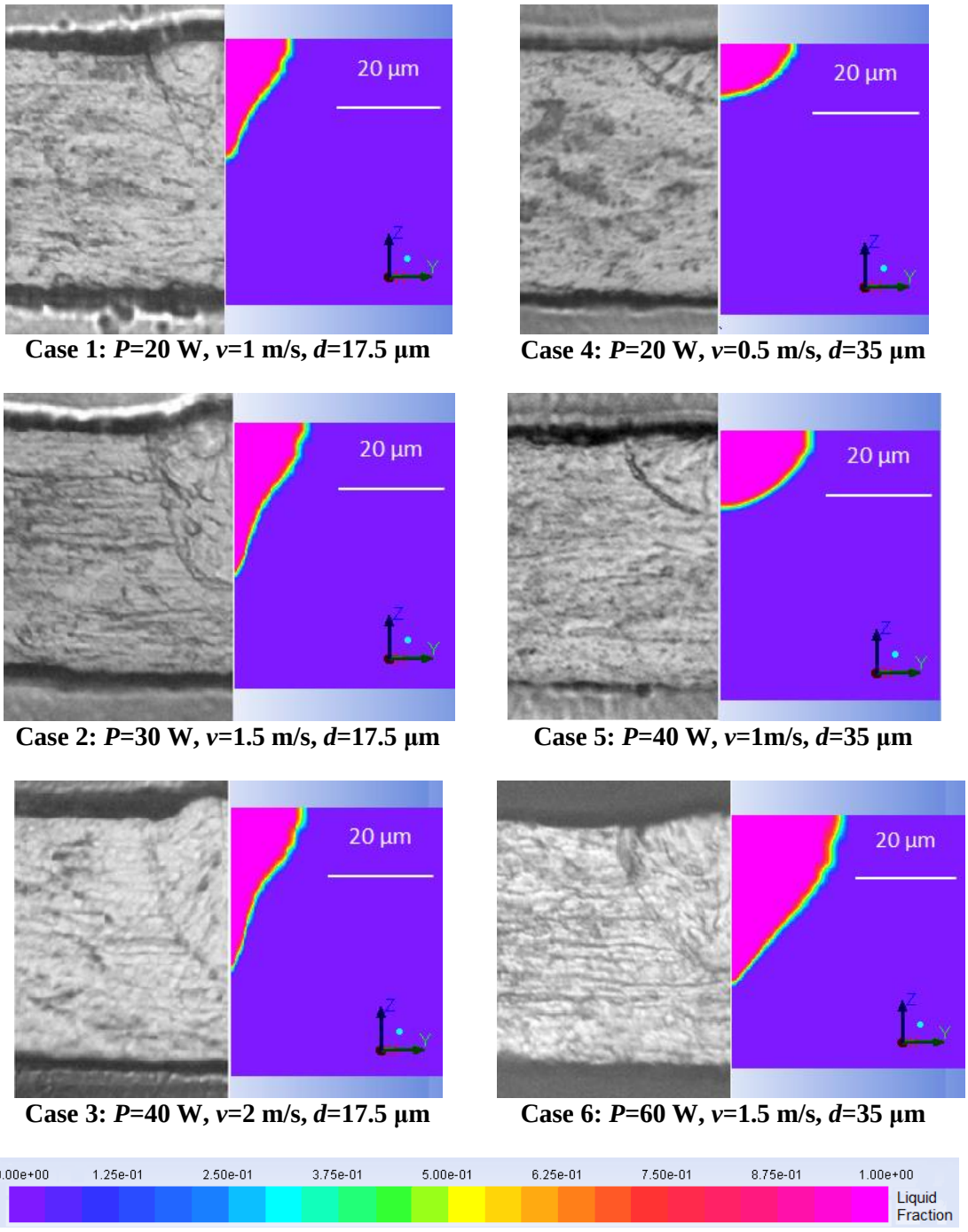

Case 1: *P*=20 W, *v*=1 m/s, *d*=17.5 µm **Case 4: *P*=20 W, *v*=0.5 m/s, *d*=35 µm**

Case 2: *P*=30 W, *v*=1.5 m/s, *d*=17.5 µm **Case 5: *P*=40 W, *v*=1m/s, *d*=35 µm**

Case 3: *P*=40 W, *v*=2 m/s, *d*=17.5 µm **Case 6: *P*=60 W, *v*=1.5 m/s, *d*=35 µm**

Fig. 14. Comparison between simulated liquid fraction and experimental result in case of weld bead geometry in cross-section view in different cases

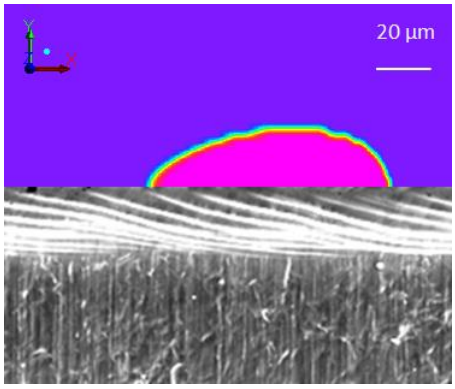

Case 1: *P*=20 W, *v*=1 m/s, *d*=17.5 µm

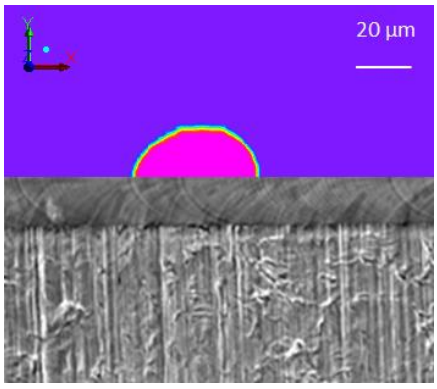

Case 4: *P*=20 W, *v*=0.5 m/s, *d*=35 µm

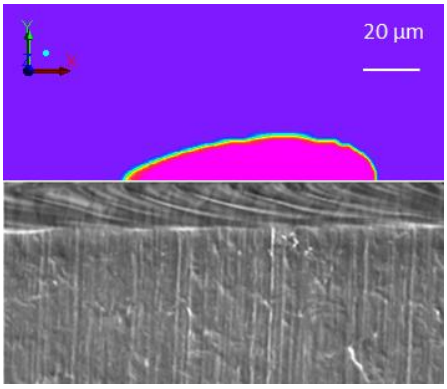

Case 2: *P*=30 W, *v*=1.5 m/s, *d*=17.5 µm

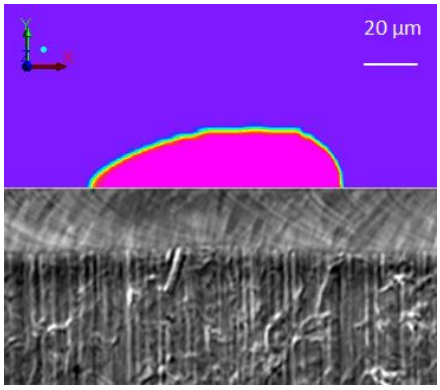

Case 5: *P*=40 W, *v*=1 m/s, *d*=35 µm

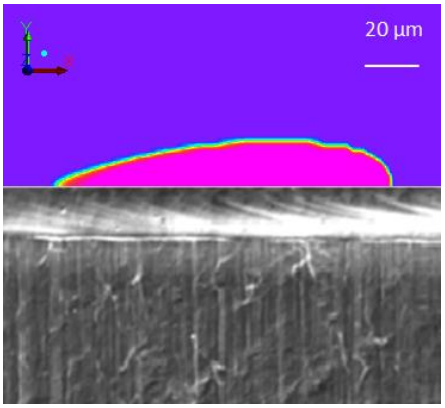

Case 3: *P*=40 W, *v*=2 m/s, *d*=17.5 µm

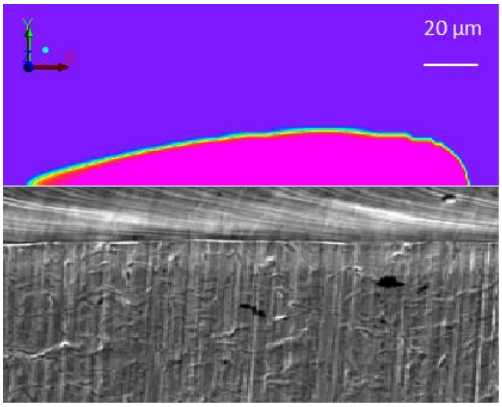

Case 6: *P*=60 W, *v*=1.5 m/s, *d*=35 µm

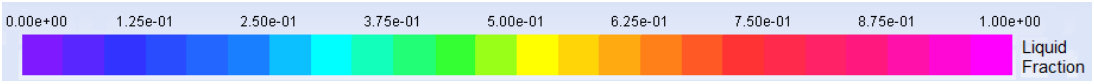

Fig. 15. Comparison between simulated liquid fraction and experimental result in case of solidification pattern from top view in different cases

The simulation results have been compared with two sets of experimental research data to predict the weld bead geometry and solidification pattern which laser welds are made on stainless steel SUS304. As can be seen, different process parameters depict different weld bead profiles and

solidification patterns. The shape comparison describes those parameters relevant to any changes in the melt dynamics and temperatures have great importance in the formation of the weld pool.

These results illustrate an acceptable prediction of the weld bead geometries and solidification patterns which exhibit an average error by employing a typical image processing software. Consequently, this model can well estimate the weld characteristics in various laser parameters and welding conditions.

4 Conclusions

The main findings and significant computed results of the present research have been represented as follows:

- The weld pool has become more elliptical shape for faster scanning velocity and higher laser power. In addition, the weld pool shape of extensive spot diameter with slower scanning velocity and lower laser power led to the circular weld pool shape.

- Both the maximum temperature and velocity of the melted metal increased with the laser power increment and the raised laser power ends up with more penetration. This computational laser micro-welding is markedly heat sensitive; accordingly, less power density induced by larger laser spot diameter, resulted in no penetration of the melt.

- At a constant laser power, the smaller size of laser beam has resulted in higher liquid metal velocity, peak temperature and weld pool depth because of greater laser power density. In contrast, with the rising of the beam diameter, lower liquid metal velocity and peak temperature have yielded, the width of the weld pool has increased and the molten pool depth decreased.

- The scale of the solidification substructure (GR) and the solidification morphology (G/R) of the fusion zone would be influenced by modifying the power of laser and diameter of laser beam in linear laser micro-welding process.

- The cooling rate (Δt_{8-5}) has been raised slightly by increasing the scanning velocity of laser, and it is also associated with laser power resulted to grow up the pick temperatures in both 17.5 μm and 35 μm spot diameters.

- Finally, having the laser micro-welds velocities in the range of 0.5 to 2 m/s, is considered as a fast mode laser welding process. Employing the maximum scanning velocity of 2 m/s will significantly improve the welding efficiency and productivity.

Acknowledgments

The authors would like to acknowledge the University of Malaya for providing the necessary facilities and resources for this research. This research was funded by the University of Malaya Postgraduate Research Grant (PPP) Program No. PG064-2016A.

References

[1] C. Brown, C. Banas, Deep penetration laser welding, in: AWS 52nd Annual Meeting, San Francisco, California, 1971.
[2] D. Majumdar, I. Manna, Laser material processing, International Materials Reviews, 56(5-6) (2011) 341-388.
[3] J.R. Berretta, W. de Rossi, M. David Martins das Neves, I. Alves de Almeida, N. Dias Vieira Junior, Pulsed Nd: YAG laser welding of AISI 304 to AISI 420 stainless steels, Optics and Lasers in Engineering, 45(9) (2007) 960-966.
[4] Z. Li, S. Gobbi, Laser welding for lightweight structures, Journal of materials processing technology, 70(1) (1997) 137-144.
[5] E. Schubert, M. Klassen, I. Zerner, C. Walz, G. Sepold, Light-weight structures produced by laser beam joining for future applications in automobile and aerospace industry, Journal of Materials Processing Technology, 115(1) (2001) 2-8.
[6] F. Malek Ghaini, M. Hamedi, M. Torkamany, J. Sabbaghzadeh, Weld metal microstructural characteristics in pulsed Nd: YAG laser welding, Scripta Materialia, 56(11) (2007) 955-958.
[7] V.A. Ventrella, J.R. Berretta, W. De Rossi, Pulsed Nd: YAG laser seam welding of AISI 316L stainless steel thin foils, Journal of Materials Processing Technology, 210(14) (2010) 1838-1843.
[8] Y. Ai, P. Jiang, X. Shao, P. Li, C. Wang, G. Mi, S. Geng, Y. Liu, W. Liu, The prediction of the whole weld in fiber laser keyhole welding based on numerical simulation, Applied Thermal Engineering, 113 (2017) 980-993.
[9] S. Pang, W. Chen, J. Zhou, D. Liao, Self-consistent modeling of keyhole and weld pool dynamics in tandem dual beam laser welding of aluminum alloy, Journal of Materials Processing Technology, 217 (2015) 131-143.
[10] Z. Yang, W. Tao, L. Li, Y. Chen, C. Shi, Numerical simulation of heat transfer and fluid flow during double-sided laser beam welding of T-joints for aluminum aircraft fuselage panels, Optics & Laser Technology, 91 (2017) 120-129.
[11] J. Liu, Z. Rao, S. Liao, H. Tsai, Numerical investigation of weld pool behaviors and ripple formation for a moving GTA welding under pulsed currents, International Journal of Heat and Mass Transfer, 91 (2015) 990-1000.
[12] R. Wang, Y. Lei, Y. Shi, Numerical simulation of transient temperature field during laser keyhole welding of 304 stainless steel sheet, Optics & Laser Technology, 43(4) (2011) 870-873.
[13] Z. Saldi, A. Kidess, S. Kenjereš, C. Zhao, I. Richardson, C. Kleijn, Effect of enhanced heat and mass transport and flow reversal during cool down on weld pool shapes in laser spot welding of steel, International Journal of Heat and Mass Transfer, 66 (2013) 879-888.
[14] A. Hozoorbakhsh, M.I.S. Ismail, N.B.A. Aziz, A computational analysis of heat transfer and fluid flow in high-speed scanning of laser micro-welding, International Communications in Heat and Mass Transfer, 68 (2015) 178-187.
[15] A. Hozoorbakhsh, M.I.S. Ismail, A.A.D.M. Sarhan, A. Bahadoran, N.B.A. Aziz, An investigation of heat transfer and fluid flow on laser micro-welding upon the thin stainless steel sheet (SUS304) using computational fluid dynamics (CFD), International Communications in Heat and Mass Transfer, 75 (2016) 328-340.
[16] M. Courtois, M. Carin, P. Le Masson, S. Gaied, M. Balabane, Guidelines in the experimental validation of a 3D heat and fluid flow model of keyhole laser welding, Journal of Physics D: Applied Physics, 49(15) (2016) 155503.

[17] X. Zhan, G. Mi, Q. Zhang, Y. Wei, W. Ou, The hourglass-like heat source model and its application for laser beam welding of 6 mm thickness 1060 steel, The International Journal of Advanced Manufacturing Technology, 88(9-12) (2017) 2537-2546.
[18] H.K. Versteeg, W. Malalasekera, An introduction to computational fluid dynamics: the finite volume method, Pearson Education, 2007.
[19] M.I.S. Ismail, Micro-welding of Engineering Materials by High Brightness Lasers, Okayama University, 2012.
[20] J. Mazumder, W. Steen, Heat transfer model for CW laser material processing, Journal of Applied Physics, 51(2) (1980) 941-947.
[21] N.S. SHANMUGAM, G. BUVANASHEKARAN, K. SANKARANARAYANASAMY, Finite Element Simulation of Nd: YAG laser lap welding of AISI 304 Stainless steel sheets, (2012).
[22] N. Sonti, M. Amateau, Finite-element modeling of heat flow in deep-penetration laser welds in aluminum alloys, Numerical heat transfer, 16(3) (1989) 351-370.
[23] T. Zacharia, S. David, J. Vitek, T. DebRoy, Weld pool development during GTA and laser beam welding of type 304 stainless steel, (1989).
[24] T. Zacharia, S. David, J. Vitek, T. Debroy, Heat transfer during Nd: YAG pulsed laser welding and its effect on solidification structure of austenitic stainless steels, Metallurgical Transactions A, 20(5) (1989) 957-967.
[25] M.A. Bramson, Infrared radiation. A handbook for applications, 1968.
[26] ANSYS Fluent 15.0 User's Manual, ANSYS Documentation>Fluent>User's Guide & Theory Guide – Release 15.0, in: ANSYS Inc., ANSYS Inc.
[27] T. DebRoy, S. David, Physical processes in fusion welding, Reviews of Modern Physics, 67(1) (1995) 85.
[28] X. He, J. Elmer, T. DebRoy, Heat transfer and fluid flow in laser microwelding, Journal of Applied Physics, 97(8) (2005) 084909.
[29] S. Kou, Welding Metallurgy, John Wiley & Sons, 2003.